Geochemistry Geophysics Geosystems G3
AN ELECTRONIC JOURNAL OF THE EARTH SCIENCES
Published by AGU and the Geochemical Society

Article
Volume 4, Number 9
12 September 2003
8615, doi:10.1029/2002GC000499
ISSN: 1525-2027

Linear analysis of melt band formation by simple shear

Marc Spiegelman
Lamont-Doherty Earth Observatory of Columbia University, Palisades, New York, 10964, USA (mspieg@ldeo.columbia.edu)

[1] Recent experiments by *Holtzman et al.* [2003] demonstrate that partially molten aggregates of many mantle materials undergoing simple shear (from ~100–500% strain) will spontaneously develop localized melt-rich bands. These bands develop at small strains but persist at low angles to the plane of shear (~15–20°) even at large shear strains. The melt-rich bands also appear to form localized weak regions that act as strain guides for the solid matrix flow. These experiments provide an opportunity to test the equations governing flow in deformable porous media developed by *McKenzie* [1984] and others. Here we present linear analysis of these equations for a solid with a porosity weakening viscosity undergoing simple shear. This analysis calculates the growth in porosity of a plane wave perturbation that initiates at an angle θ_0 to the plane of shear after some amount of finite strain. For a strain of 300%, the maximum growing melt band initiates at 16.8° (but rotates to ~70° in the linear analysis). We also calculate the additional solid shear induced by the localized weak regions and show that it develops a sense of shear consistent with observations only for melt bands less that 45°. These two results suggest that only low angle bands are favored under shear, consistent with the observations. The linear analysis, however, does not allow the porosity growth and shear to interact which causes the initially low angle bands to be rotated to higher angles by the background simple shear. To follow the further development of the bands requires solutions of the full nonlinear equations. Nevertheless, the linear analysis provides useful insights into the development of the shear bands and suggests that the theory is useful for describing partially molten systems.

Components: 5195 words, 8 figures.

Keywords: Melt localization; deformable porous media; linear analysis.

Index Terms: 8434 Volcanology: Magma migration; 3210 Mathematical Geophysics: Modeling.

Received 19 December 2002; **Revised** 6 June 2003; **Accepted** 11 June 2003; **Published** 12 September 2003.

Spiegelman, M., Linear analysis of melt band formation by simple shear, *Geochem. Geophys. Geosyst.*, *4*(9), 8615, doi:10.1029/2002GC000499, 2003.

Theme: The Oman Ophiolite and Mid-Ocean Ridge Processes
Guest Editors: Peter Kelemen, Chris MacLeod, and Susumu Umino

1. Introduction

[2] Understanding the dynamics and properties of partially molten regions has been a goal of experimentalists, theorists, and observationalists for some time now. An outstanding challenge, however, has been to integrate these different techniques. Recent experiments on the deformation of partially molten materials [e.g., *Zimmerman et al.*, 1999; *Renner et al.*, 2003; *Holtzman et al.*, 2003] provide

an important opportunity for consolidating experiment and theory because these experiments should be describable using the prevailing macroscopic theory for partially molten materials [*McKenzie*, 1984; *Scott and Stevenson*, 1984; *Fowler*, 1985; *Scott and Stevenson*, 1986; *Scott*, 1988; *Spiegelman*, 1993a, 1993b; *Bercovici et al.*, 2001a; *Ricard et al.*, 2001; *Bercovici et al.*, 2001b]. Directly testing and calibrating the theory against physical experiments should allow us to extrapolate laboratory conditions to the mantle and help design new and diagnostic experiments.

[3] Here we are motivated by a set of experiments by *Zimmerman et al.* [1999] and *Holtzman et al.* [2003] that demonstrate that partially molten aggregates can spontaneously develop localized "melt-rich bands" that form at small strains and low angles to the plane of shear ($\sim$15–20°) and persist at these low angles even in samples deformed to large strains of 200–500% (Figures 1 and 2). Theory suggests that the intrinsic length scale in partially molten systems is the compaction length $\delta = \sqrt{k_\phi(\zeta + 4\eta/3)/\mu}$ [e.g., *McKenzie*, 1984; *Spiegelman*, 1993a, 1993b] which depends on the permeability, k_ϕ, and the ratio of solid viscosities ($\zeta + 4\eta/3$) and melt viscosity μ. Owing to uncertainties in all of these quantities (particularly the permeability), the exact compaction length of any sample is difficult to determine. However, by varying the material properties of both melt and solid phases, the experimenters varied the relative compaction length of the sample with respect to the size of the experiment and suggested that the melt bands form in systems larger than the compaction length. The authors state that in all band-forming experiments, there was a distribution of bands with fewer large bands and more numerous, more closely spaced smaller bands between them. The authors measure the distance between the "largest melt bands," and while acknowledging that this is somewhat subjective, argue that there is a preferred inter-band spacing of approximately 0.15–0.2δ.

[4] These melt segregations are suggestive of those calculated by *Stevenson* [1989] for a system undergoing pure shear. To test this idea, we revisit his calculation for the problem of simple shear and show that the theory provides useful insights into the behavior of the experiments.

2. Governing Equations

[5] The analysis follows closely that of *Stevenson* [1989] and begins with the equations for conservation of mass and momentum of a two phase mixture of melt in a deformable matrix with variable shear viscosity. Neglecting melting, and assuming the solid and liquid densities (ρ_s, ρ_f) are constant, these equations can be written dimensionally as

$$\frac{\partial \phi}{\partial t} + \nabla \cdot [\phi \mathbf{v}] = 0 \tag{1}$$

$$\frac{\partial}{\partial t}(1-\phi) + \nabla \cdot [(1-\phi)\mathbf{V}] = 0 \tag{2}$$

$$\phi(\mathbf{v} - \mathbf{V}) = -\frac{k_\phi}{\mu}\left[\nabla P - \rho_f \mathbf{g}\right] \tag{3}$$

$$\nabla P = \nabla \cdot \eta\left[(\nabla \mathbf{V}) + (\nabla \mathbf{V})^T\right] + \nabla\left(\zeta - \frac{2\eta}{3}\right)\nabla \cdot \mathbf{V} + \bar{\rho}\mathbf{g} \tag{4}$$

where ϕ is the porosity, $\mathbf{v}$, $\mathbf{V}$ are the melt and solid velocities, $k_\phi = k_0\phi^n$ is the permeability, which is assumed to be a nonlinear increasing function of porosity. P is the fluid pressure, $\mathbf{g}$ is the acceleration due to gravity, $\nabla\mathbf{V}$ is the velocity gradient tensor whose i,jth component is $\partial V_i/\partial x_j$, ζ and η are the matrix bulk and shear viscosities respectively and $\bar{\rho} = [\rho_s(1-\phi) + \rho_f\phi]$ is the mean density of the two-phase mixture. For these problems we assume that the viscosity is only a function of porosity and is porosity weakening [*Hirth and Kohlstedt*, 1995a, 1995b; *Mei et al.*, 2002].

[6] If the porosity (and therefore the viscosity) is constant, however, and melting is neglected, *Spiegelman and McKenzie* [1987] and *Spiegelman* [1993a] show that these equations reduce to the problem of solving only for the incompressible flow of the solid. For the case of a constant

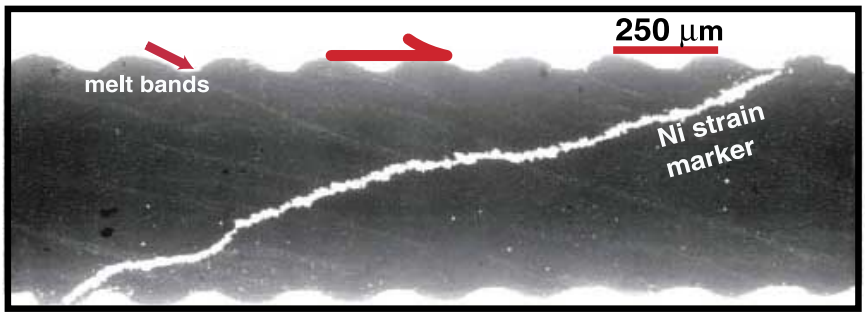

Figure 1. Figure and description courtesy of B.K Holtzman et al. for experiments described in Holtzman et. al (submitted manuscript, 2003). These experiments show the development of melt-rich bands in an anorthite/MORB aggregate sheared to a strain of ~300%. In this reflected light image, the melt-rich bands appear as whitish streaks aligned from 10–20° from the shear plane. As pointed out by *Holtzman et al.* [2003], some of the bands are clearly nucleating off the serations in the sample wall, however, while in some regions, every groove has an associated band, not every band has a groove. Moreover, similar bands formed in other experiments with polished olivine walls and no serations.

porosity medium undergoing simple shear, the solid velocity field is

$$\mathbf{V}_0 = \dot{\gamma} y \mathbf{i} \tag{5}$$

where $\dot{\gamma} = \partial U_0/\partial y$ is the constant shear strain rate.

[7] We now consider the behavior of infinitesimal perturbations to this basic state in the absence of gravity (which should have small effects in these experiments). To develop equations for these perturbations, we first rewrite equations (1)–(4) as

$$\frac{\partial \phi}{\partial t} + \mathbf{V} \cdot \boldsymbol{\nabla} \phi = (1 - \phi)\mathcal{C} \tag{6}$$

$$\mathcal{C} = \nabla \cdot \frac{k_\phi}{\mu} \left[\boldsymbol{\nabla} \cdot \eta \left[\boldsymbol{\nabla}\mathbf{V} + \boldsymbol{\nabla}\mathbf{V}^T \right] + \boldsymbol{\nabla} \left(\zeta - \frac{2\eta}{3} \right) \mathcal{C} \right] \tag{7}$$

$$0 = \boldsymbol{\nabla} \times \left(\boldsymbol{\nabla} \cdot \left[\eta \left(\boldsymbol{\nabla}\mathbf{V} + \boldsymbol{\nabla}\mathbf{V}^T \right) \right] \right) \tag{8}$$

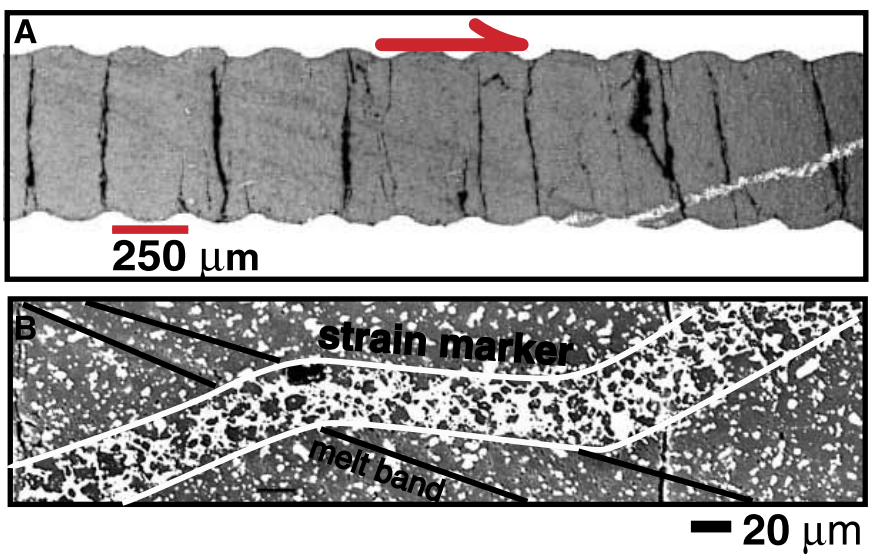

Figure 2. Additional figures for experiments described in *Holtzman et al*. [2003]. (a) Olivine + chromite + 2 vol% MORB sample deformed to a shear strain of ~350%. The white grains are chromite, the gray matrix is olivine plus fine-grained chromite, and the slightly darker streaks are the melt-rich bands, oriented ~20° from the piston wall. A portion of the Ni strain marker is visible in the lower right corner. The fractures normal to the piston walls were created during quenching. The bands in this sample with 2% MORB are generally narrower, more closely spaced, and more numerous than those in the samples with 6 and 12% MORB. (b) In a sample with 12% MORB, the Ni strain marker is offset in a right-lateral sense caused by deformation on a melt-rich band with the same sense of shear as the overall sample deformation. This image was taken in SEM. Figure courtesy of B.K. Holtzman et al.

where $\mathcal{C} = \nabla\cdot\mathbf{V}$ is the isotropic strain rate or "compaction rate." Equation (6) is the expansion of equation (2) and shows that changes in porosity are caused by advection by the solid flow and compaction/expansion of the matrix. Equation (7) combines equations (1)–(4) to show that volume changes of the matrix result from the divergence of the melt flux. In the absence of gravity, this flux is driven solely by pressure gradients caused by viscous deformation. Finally, equation (8) is the curl of equation (4) and controls incompressible flow of the solid. *Spiegelman* [1993a] presents this decomposition in more detail.

[8] We now consider the behavior of infinitesimal perturbations to the constant porosity state by letting

$$\begin{aligned}\phi &= \phi_0 + \varepsilon\phi_1\\ \mathcal{C} &= 0 + \varepsilon\mathcal{C}_1\\ \mathbf{V} &= \dot{\gamma}y\mathbf{i} + \varepsilon\left(\nabla\times\psi_1^s\mathbf{k} + \nabla\mathcal{U}_1\right)\\ k_\phi &= k_0 + \varepsilon k_1\\ \eta &= \eta_0 + \varepsilon\eta_1\end{aligned} \tag{9}$$

Here we have decomposed the perturbed solid velocity $\mathbf{V}_1 = \nabla\times\psi_1{}^s\mathbf{k} + \nabla\mathcal{U}_1$ into its incompressible and compressible components. Substituting into equations (6)–(8) and collecting terms of order ε yields, after a bit of algebra, the equations for the perturbations

$$\frac{\partial\phi_1}{\partial t} + \dot{\gamma}y\frac{\partial\phi_1}{\partial x} = (1-\phi_0)\mathcal{C}_1 \tag{10}$$

$$-\delta^2\nabla^2\mathcal{C}_1 + \mathcal{C}_1 = 2\dot{\gamma}\frac{\delta^2}{(\zeta_0 + 4\eta_0/3)}\frac{\partial^2\eta_1}{\partial x\partial y} \tag{11}$$

$$\nabla^2\mathcal{U}_1 = \mathcal{C}_1 \tag{12}$$

$$\nabla^2\left(\nabla^2\psi_1^s\right) = \frac{\dot{\gamma}}{\eta_0}\left(\frac{\partial^2\eta_1}{\partial x^2} - \frac{\partial^2\eta_1}{\partial y^2}\right) \tag{13}$$

where $\delta = [k_0(\zeta_0 + 4\eta_0/3)/\mu]^{1/2}$ is the compaction length at the reference porosity ϕ_0. Equation (10) states that changes in porosity will be controlled by advection by the simple shear flow and any compaction or expansion of the solid. Equations (11) and (13) state that compaction and the incompressible shear flow are driven by simple shear, $\dot{\gamma}$, interacting with variations in the shear viscosity, η. Equation (12) calculates the compressible velocity field given the compaction rate and follows directly from the definitions of $\mathcal{C}$ and $\mathcal{U}$.

[9] To close these equations requires a relationship between the perturbed shear viscosity and the other first order variables. Here we assume that the shear viscosity is only a function of porosity $\eta(\phi) = \eta_0 f(\phi)$ (where $f(\phi_0) = 1$). Therefore the order ε term of the Taylor expansion of $\eta(\phi_0 + \varepsilon\phi_1)$ is $\eta_1 = \eta_0\alpha\phi_1$ where $\alpha = df/d\phi(\phi_0)$. Note that α is negative for a porosity weakening material.

[10] This derivation is independent of the functional form of the viscosity $\eta(\phi)$. On the basis of a compilation of published creep experiments, however, *Kelemen et al.* [1997] suggested that $\eta(\phi) = \eta_d e^{-\beta\phi}$ where η_d is the shear viscosity of melt free systems (which can be a function of temperature, pressure and stress). *Kelemen et al.* [1997] used $\beta = 45$ although (Holtzman et al., submitted manuscript, 2003) suggest $\beta = 25$ based on more recent experiments [*Mei et al.*, 2002]. This functional form gives $\alpha \sim -\beta$ which is clearly porosity weakening.

[11] Finally, we nondimensionalize equations (10)–(13) using the scaling

$$\begin{aligned}t &= \frac{1}{\dot{\gamma}}t' \qquad \mathbf{x} = \delta\mathbf{x}'\\ \mathcal{C}_1 &= \dot{\gamma}\mathcal{C}_1' \quad \left(\psi_1^s, \mathcal{U}_1\right) = \dot{\gamma}\delta^2\left(\psi_1^s, \mathcal{U}_1\right)'\end{aligned} \tag{14}$$

Here, time is scaled by the strain rate $\dot{\gamma}$ such that the dimensionless time $t' = \dot{\gamma}t$ is just the total strain. Distance is scaled by the compaction length δ. Substituting this scaling and $\eta_1 = \eta_0\alpha\phi_1$ into equations (10)–(13) and dropping primes yields

$$\frac{\partial\phi_1}{\partial t} + y\frac{\partial\phi_1}{\partial x} = (1-\phi_0)\mathcal{C}_1 \tag{15}$$

$$-\nabla^2\mathcal{C}_1 + \mathcal{C}_1 = 2\alpha\xi\frac{\partial^2\phi_1}{\partial x\partial y} \tag{16}$$

$$\nabla^2\mathcal{U}_1 = \mathcal{C}_1 \tag{17}$$

$$\nabla^4\psi_1^s = \alpha\left(\frac{\partial^2\phi_1}{\partial x^2} - \frac{\partial^2\phi_1}{\partial y^2}\right) \tag{18}$$

where $\xi = \eta_0/(\zeta_0 + 4\eta_0/3) = O(1)$. Note that in this scaling the behavior is independent of strain rate and only depends on α.

3. Solutions-Infinite Domains

[12] For the case of infinite domains, equations (15)–(18) have analytic solutions that provide useful insights into the process of melt-band formation. We present two solutions here. The first is for general perturbations to a constant viscosity flow which demonstrates that arbitrary perturbations are only sheared by the background flow if there is no feedback between porosity and viscosity. This solution, however, helps set up the more general solution for plane wave perturbations in a porosity weakening flow which can grow unstably into melt-rich bands.

3.1. Constant Viscosity, Time-Dependent Solutions ($\alpha = 0$)

[13] For constant viscosity, time-dependent flows, $\alpha = 0$ which admits solutions $\mathcal{C}_1 = \mathcal{U}_1 = \psi_1{}^s = 0$ for boundary conditions where these perturbations vanish as $||\mathbf{x}|| \rightarrow \infty$. Under these conditions, equations (15)–(18) reduce to just a single equation for porosity

$$\frac{\partial \phi_1}{\partial t} + y\frac{\partial \phi_1}{\partial x} = 0 \tag{19}$$

Equation (19) can be solved by the method of characteristics [e.g., *Whitham*, 1974] to give the general solution

$$\phi_1(x, y, t) = f(x - yt, y) \tag{20}$$

where f is an arbitrary function that satisfies the initial condition $\phi_1(x_0, y_0, 0) = f(x_0, y_0)$. Equation (20) is just shear of a function along horizontal planes. An example that is useful for the next section is an infinite plane wave with initial wave vector $\mathbf{k}_0 = k_x^0\mathbf{i} + k_y^0\mathbf{j}$, such that the initial condition $\phi_1(\mathbf{x}, 0) = \exp(i\mathbf{k}_0 \cdot \mathbf{x})$ becomes

$$\phi_1(\mathbf{x}, t) = \exp\left[i\left(k_x^0(x - yt) + k_y^0 y\right)\right] = \exp[i\mathbf{k}(t) \cdot \mathbf{x}] \tag{21}$$

where

$$\mathbf{k}(t) = k_x^0\mathbf{i} + \left(k_y^0 - k_x^0 t\right)\mathbf{j} \tag{22}$$

is a time-dependent wave vector that rotates with the flow and changes length. For example, a perturbation oriented like the melt bands has an initial wave vector with $k_y^0 > k_x^0 > 0$. In this case, $\mathbf{k}$ initially reduces in length and the wavelength appears to increase (see Figures 3a and 3b).

3.2. Nonconstant Viscosity Solutions

[14] Given solutions for plane waves with $\alpha = 0$, we now seek solutions for the full linearized equations of the form

$$\phi_1 = \exp[i\mathbf{k}(t) \cdot \mathbf{x} + s(t)] \tag{23}$$

$$\mathcal{C}_1 = \mathcal{C}^*(t)\exp[i\mathbf{k}(t) \cdot \mathbf{x} + s(t)] \tag{24}$$

$$\mathcal{U}_1 = \mathcal{U}^*(t)\exp[i\mathbf{k}(t) \cdot \mathbf{x} + s(t)] \tag{25}$$

$$\psi_1^s = \psi^*(t)\exp[i\mathbf{k}(t) \cdot \mathbf{x} + s(t)] \tag{26}$$

where $\mathbf{k}(t)$ is given by equation (22) and $e^{s(t)}$ is the amplitude of the porosity plane wave after time t.

[15] Substituting equations (23)–(24) into (15)–(16) yields a set of equations for the time-dependent amplitudes

$$\frac{ds}{dt} = -2\alpha\xi(1 - \phi_0)\frac{k_x k_y}{k^2 + 1} \tag{27}$$

$$\mathcal{C}^*(t) = -2\alpha\xi\frac{k_x k_y}{k^2 + 1} \tag{28}$$

$$\mathcal{U}^*(t) = -\mathcal{C}^*(t)/k^2 \tag{29}$$

$$\psi^*(t) = \alpha\frac{k_y^2 - k_x^2}{k^4} \tag{30}$$

where $k^2(t) = \mathbf{k} \cdot \mathbf{k}$.

[16] Equation (27) can be integrated directly for $s(t)$

$$s(t) = -2\alpha\xi(1 - \phi_0)\int_0^t \frac{\left(k_y^0 - k_x^0 t\right)}{\left(k_x^0\right)^2 + 1 + \left(k_y^0 - k_x^0 t\right)^2} k_x^0 dt \tag{31}$$

to yield

$$s(t) = -\alpha\xi(1 - \phi_0)\ln\left[\frac{1 + k^2(0)}{1 + k^2(t)}\right] \tag{32}$$

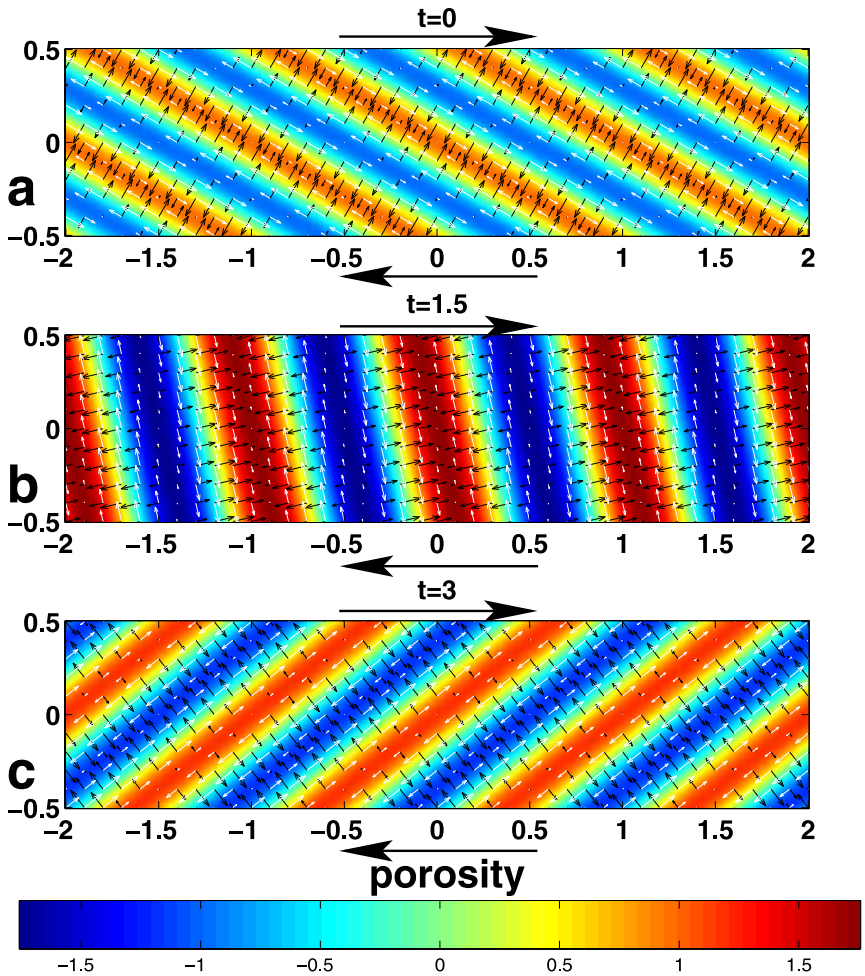

Figure 3. Linearized solution for the evolution of porosity, melt flux and enhanced solid shear for a plane wave perturbation with initial wavenumber $k = 4\pi$ and initial angle $\theta_0 = 30°$ from the horizontal shear plane. Here the shear viscosity is only mildly porosity weakening ($\alpha = -1$) to be able to track the perturbations to high strains. Colored fields show porosity. Black arrows show perturbed melt flow vectors, and white arrows show the perturbed solid velocity field. Time t is total strain. Simple shear rotates the initial perturbation while increasing its wavelength (decreasing k) up to $\theta = 90°$. Beyond 90° the wavelength decreases. If the viscosity is also porosity weakening, then the initial rotation causes the high porosity regions to have a lower pressure which sucks in melt causing the melt bands to grow in porosity. Melt is expelled from the bands at angles greater than 90°. Variable shear viscosity also causes additional solid flow parallel to the melt bands. The sense of shear, however, changes sign at 45,135,225 and 315°.

Therefore the amplitude of the plane wave at time t is

$$A(t) = e^{s(t)} = \left[\frac{1 + k^2(0)}{1 + k^2(t)}\right]^{-\alpha\xi(1-\phi_0)} \tag{33}$$

which depends only on α and the wave number at time t relative to its initial value, not the orientation of the wave. It is the rotation by simple shear that drives the change in wave number.

[17] For illustration, Figure 3 shows one solution of these equations for an initial perturbation that begins at $\theta = 30°$ with a wave number $k = 4\pi$ (and $\alpha = -1$). As in the constant viscosity case, these bands rotate in the shear, however, a porosity weakening viscosity ($\alpha < 0$) causes the amplitude of the perturbation to initially grow. Variable viscosity also causes additional shear along the porosity bands. The growth of perturbations and

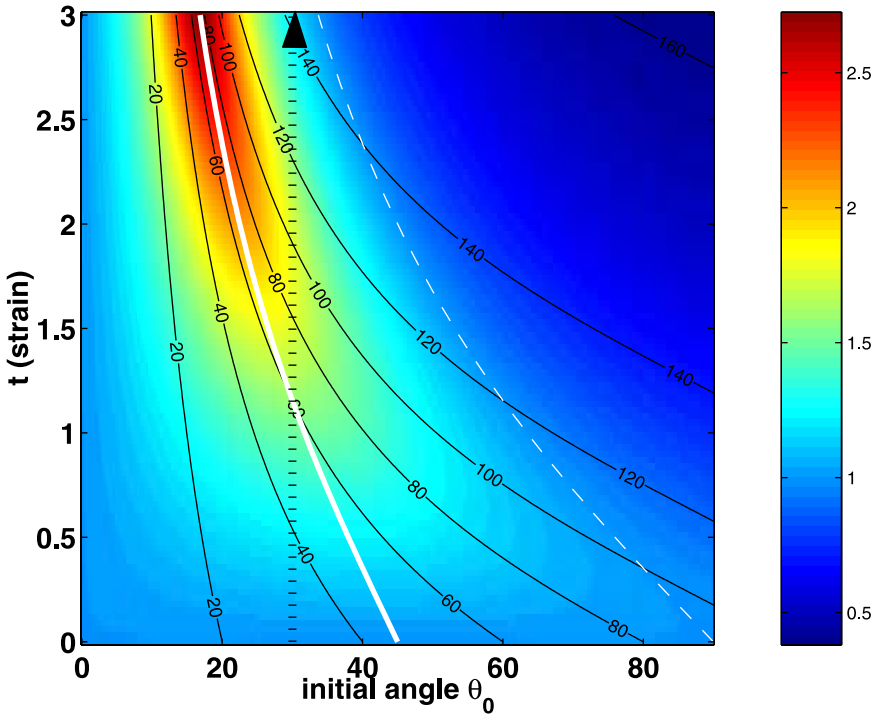

Figure 4. Plane wave amplitude $A(t, \theta_0)$ (equations (33) and (34)) as a function of time (strain) and initial angle for $\alpha = -1$. The colored field shows $A(t, \theta_0)$ for a high frequency plane wave ($k(0) = 4\pi$) as in Figure 3. The thick white curve shows $\theta_{max}(t)$ (equation (35)). The dashed white line is $2\theta_{max}$. The black contours show the final angle achieved at time t and the black dotted arrow shows the trajectory of the plane wave illustrated in Figure 3 that starts at $\theta_0 = 30°$ and ends around $\theta_f = 140°$. However, the wave that grows the most by $t = 3$ is the wave that initiates around 17° and rotates to about 70°. More strongly porosity weakening systems have more negative values of α and grow to larger amplitudes faster. However, changing α only scales the magnitude of this image, not the angular dependence.

the additional shear are decoupled in the linearized solutions (although probably not in the full solutions) and can be discussed separately.

3.2.1. Growth of Melt Bands

[18] Equation (27) gives the instantaneous growth rate of a plane wave with wave vector **k**. For a porosity-weakening shear viscosity ($\alpha < 0$), growth is positive for all wave vectors with k_x, $k_y > 0$. If we write the components of the wave vectors as $k_x = k \sin\theta$, $k_y = k \cos\theta$ where $k = ||\mathbf{k}||$ and θ is the angle that the wave makes with the shear plane, it is clear that all waves with angles $0 < \theta < 90°$ increase in amplitude while those with $90 < \theta < 180°$ decrease. The maximum instantaneous growth rate occurs for $\theta = 45°$ which is the maximum opening direction in simple shear. However, because these waves continue to rotate in time, initially fast growing waves will get rotated out of their favorable position (and may eventually reduce in amplitude) after a finite amount of strain. Thus for large strains, the waves that demonstrate the largest amount of growth after a fixed time all initiate at angles smaller than 45°. The initial angle, θ_0, of the largest growing wave is apparent in Figure 4 which plots $A(t, \theta_0)$. This angle can be found by noting that in the limit $k \gg 1$, the amplitude is independent of k and simplifies to

$$A(t,\theta_0) \rightarrow \left[\frac{1}{\sin^2\theta_0 + (\cos\theta_0 - t\sin\theta_0)^2}\right]^{-\alpha\xi(1-\phi_0)} \tag{34}$$

which has a maximum at time t for initial angle

$$\theta_{max}(t) = \frac{1}{2}\tan^{-1}\frac{2}{t} \tag{35}$$

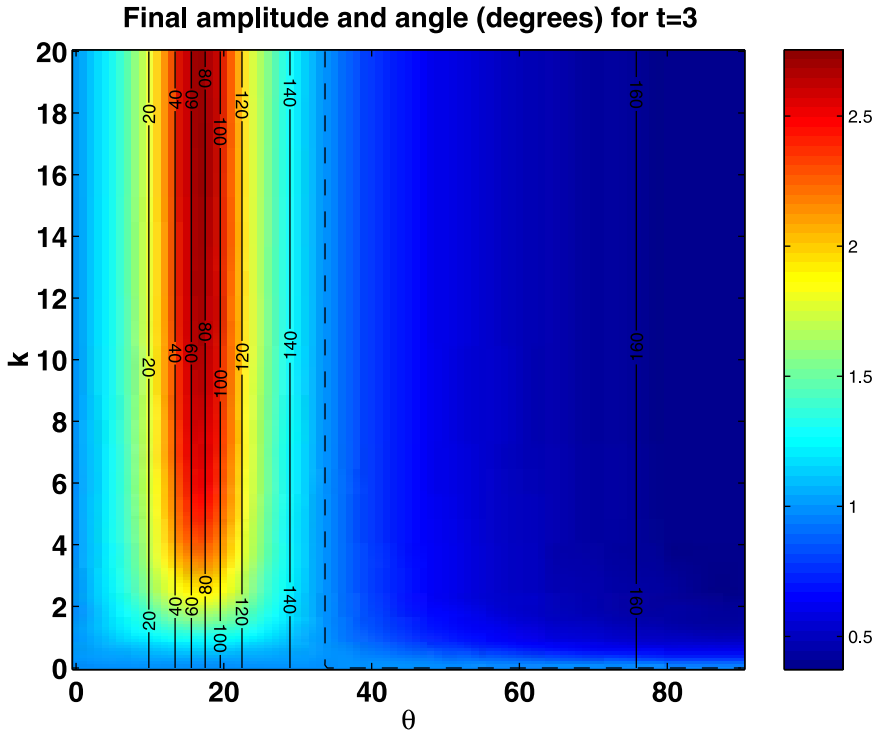

Figure 5. Final amplitude and angle after a dimensionless time of $t = 3$ as a function of initial angle and initial wavenumber. The amplitude is given in the colored background; the final angles as numbered solid contours. Maximum growth occurs for all wavenumbers $\gtrsim 2\pi$ (wavelengths smaller than the compaction length) that initiate at angles of $\theta_{max} = 16.8°$. There is no largest growing wavenumber in this analysis. The dashed lines shows the contour for no growth, $A(t) = 1$.

This analysis also shows that only initial angles less than $2\theta_{max}$ grow at all. Initial angles greater than this eventually decrease in amplitude. For a total strain of 3, ($\theta_{max} = 16.8°$), waves that initiate around 17° to the shear plane show the most growth. (Figures 4 and 5).

[19] Figure 4 is calculated for a single initial wave number $k = 4\pi$. Figure 5, however, shows how amplitude depends on wave number by plotting the amplitude at a fixed time ($t = 3$) as a a function of initial angle and initial wave number $k(0)$. Again, the maximum amplitude is attained for waves that start around 17° for all waves with $k(0) \gtrsim 2\pi$ (i.e., wavelengths shorter than a compaction length). Longer wavelengths grow more slowly, however, there is no obvious "fastest" growing wave in this analysis.

[20] The physical basis for the growth of porosity becomes clear when we consider the perturbed separation flux $(\mathbf{v}_1 - \mathbf{V}_1) = -\nabla P_1$ where

$$\nabla P_1 = \xi \nabla \times \nabla^2 \psi_1^s \mathbf{k} + \nabla \mathcal{C}_1 + \alpha \xi \mathrm{R} \nabla \phi_1 \qquad (36)$$

Equation (36) is the perturbed pressure gradient which is controlled by three terms. The first term describes pressure gradients induced by incompressible shear (ψ_1^s). These gradients are parallel to the wave fronts, however and do not induce growth. The second term describes pressure gradients due to viscous volume changes ($\mathcal{C}_1$) which are oriented normal to the wave fronts. These gradients, however, actually drive fluid out of the melt bands. It is the final term that controls the growth of the porosity bands and describes the pressure gradients induced by shear across viscosity variations. Here

$$\mathrm{R} = \begin{bmatrix} 0 & 1 \\ 1 & 0 \end{bmatrix}$$

is the reflection matrix that maps (k_x, k_y) to (k_y, k_x) by reflecting around a plane oriented at 45 degrees. The final term in equation (36) dominates the perturbed fluid flow and draws melt into the low-

angle melt bands if the viscosity is porosity weakening ($\alpha < 0$). Figure 3 also shows the instantaneous melt flux vectors $\mathbf{v}_1$, aft different times. Note that when $\theta < 90°$ the perturbed melt flux goes into the melt-bands while for $\theta > 90°$ melt is expelled.

[21] This solution is similar to that of *Stevenson* [1989] for pure shear, however, his solution purposely neglects advection of the perturbation by the background solid flow. In the case of pure shear, this approximation is reasonable, however, for simple shear, it is the rotation of weak melt-rich bands that is responsible for their growth. These linearized solutions rotate significantly more than the observed melt-rich bands, however, these solutions still provide some clue as to the behavior of the fully nonlinear problem.

3.2.2. Enhanced Matrix Shear

[22] In these linearized solutions, the rotation is driven by the zeroth order flow field which is not modified by the growing perturbations. In the experiments, however, it is clear that once the melt bands attain a sufficiently large porosity, they become weak regions that act as strain guides for matrix shear (that may actually reduce or stop the rotation). Some of this behavior, however, is captured in the linearized solutions. The perturbed stream function ψ_1^s, has the same functional form as the porosity. Therefore, streamlines will be coincident with porosity contours implying solid flow along the bands. In particular, for a porosity weakening viscosity, the perturbed solid flow $\mathbf{V}_1 = \nabla \times \psi_1^s \mathbf{k}$ produces a right-lateral shear across the melt bands (as is seen in the experiments) for melt bands at angles $0 < \theta < 45°$ (Figure 3a). For angles between 45 and 135°, the sense of shear is reversed (Figure 3b). Figure 6 summarizes all the possible combinations of melt and solid flow velocities for perturbations in different orientations. Only low angle perturbations at angles less than 45° from the shear plane both grow and have a sense of shear across them that is consistent with and enhances the zeroth order simple shear. This orientation is the one seen in the experiments.

[23] A more quantitative measure of the shear is the perturbed vorticity, $\boldsymbol{\omega}_1 = -\nabla^2 \psi_1^s \mathbf{k}$. For simple shear, the zeroth order vorticity is constant and negative for right-lateral shear (i.e., $\boldsymbol{\omega}_0 = -\dot{\gamma}\mathbf{k}$). It is useful to define the enhanced shear rate as

$$S(t) = \frac{\boldsymbol{\omega}_1 \cdot \boldsymbol{\omega}_0}{\| \boldsymbol{\omega}_0 \|} = -\alpha \frac{\left(k_y^2 - k_x^2\right)}{k^2} A(t) \tag{37}$$

which is the magnitude of the perturbed vorticity in the direction of the background vorticity. $S(t)$ is positive when the perturbed shear is in the same direction as the applied shear, and negative when opposed. Figure 7 shows the enhanced shear as a function of initial angle and time for a more strongly porosity weakening material with $\alpha = -25$. The amplitude of the perturbation grows rapidly in this problem so that it increases by two orders of magnitude by $t = \sim 0.65$. Beyond this time, the assumption of a small perturbation is probably questionable. Figure 7 shows that only waves at angles <45° have the correct sense of shear with a maximum value of $S(t)$ for waves around ~30°. Waves steeper than 45° have a sense of shear opposed to the background. The most negative shear occurs for waves oriented at ~60° with a rate of opposing shear that is ~3 times larger than that for the low angle waves. If the selection of the preferred angle of the melt-rich bands depends on shear as well as porosity growth, it suggests that higher angle perturbations may be suppressed.

[24] The shear rate can be compared to the growth rate for the same problem

$$\sigma(t) = \frac{dA}{dt} = -2\alpha\xi(1 - \phi_0) \frac{k_x k_y}{k^2 + 1} A(t) \tag{38}$$

which is approximately the same magnitude as $S(t)$ (i.e., both are of order $\alpha A(t)$). Figures 8a and 8b compares the shear rate to the growth rate where each is normalized by the largest positive rate at any given time. The fastest shearing waves occur at low angles $\theta = 20–30°$ while the fastest growing waves occur around 45° (but have negligible shear). Figure 8c shows the product of the

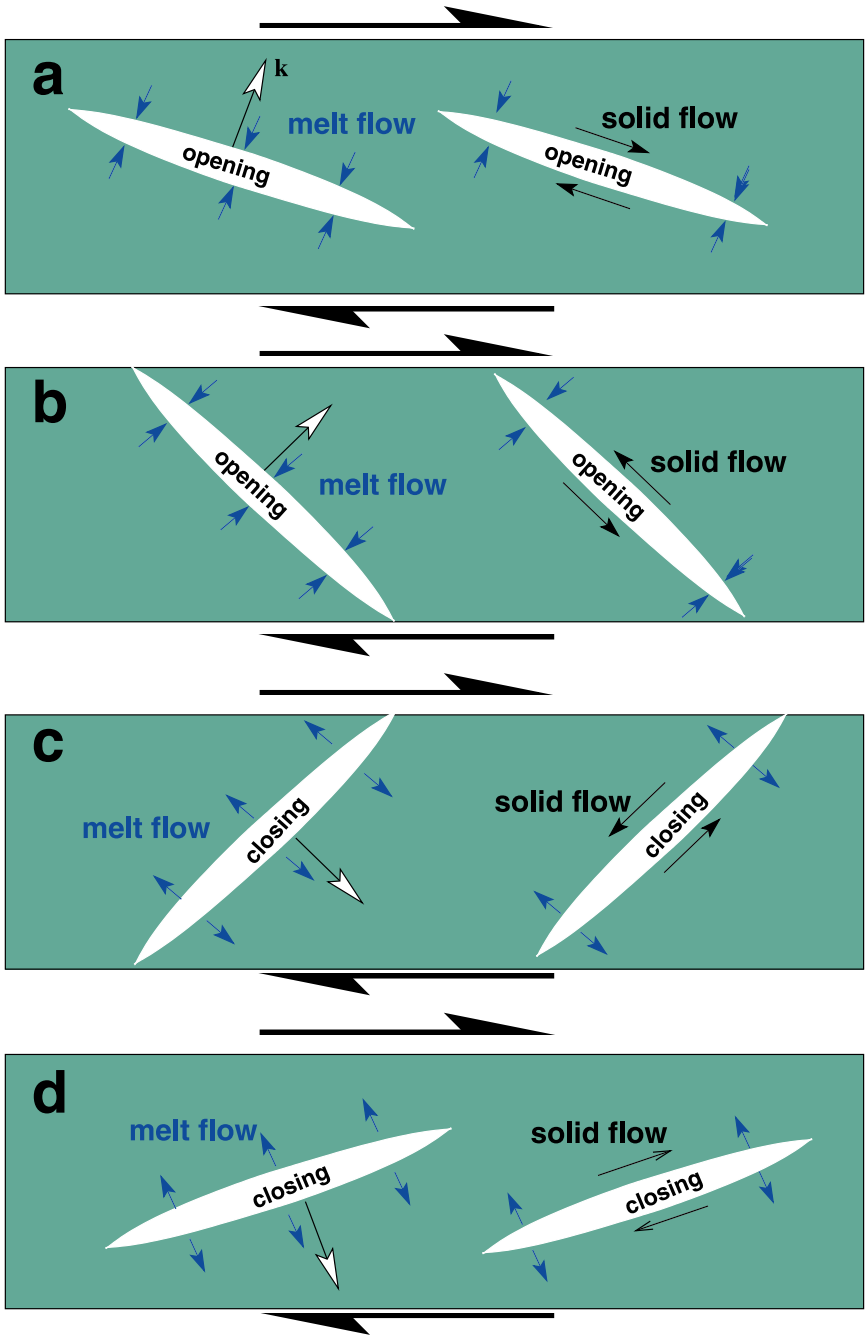

Figure 6. Summary cartoon showing qualitative behavior of the linearized solutions for perturbations in four different orientations with a porosity weakening viscosity ($\alpha < 0$). (a) $0 < \theta < 45°$. Low angle perturbations grow in porosity and develop a right-lateral sense of solid shear across them. (b) $45 < \theta < 90°$ Higher angle perturbations still grow, but the sense of solid shear is reversed. (c) $90 < \theta < 135°$ Perturbations at angles greater than 90° close up (and here have a reversed sense of shear). (d) these perturbations will enhance shear but continue to close. Only low-angle perturbations (configuration Figure 5a) both grow and enhance the solid shear.

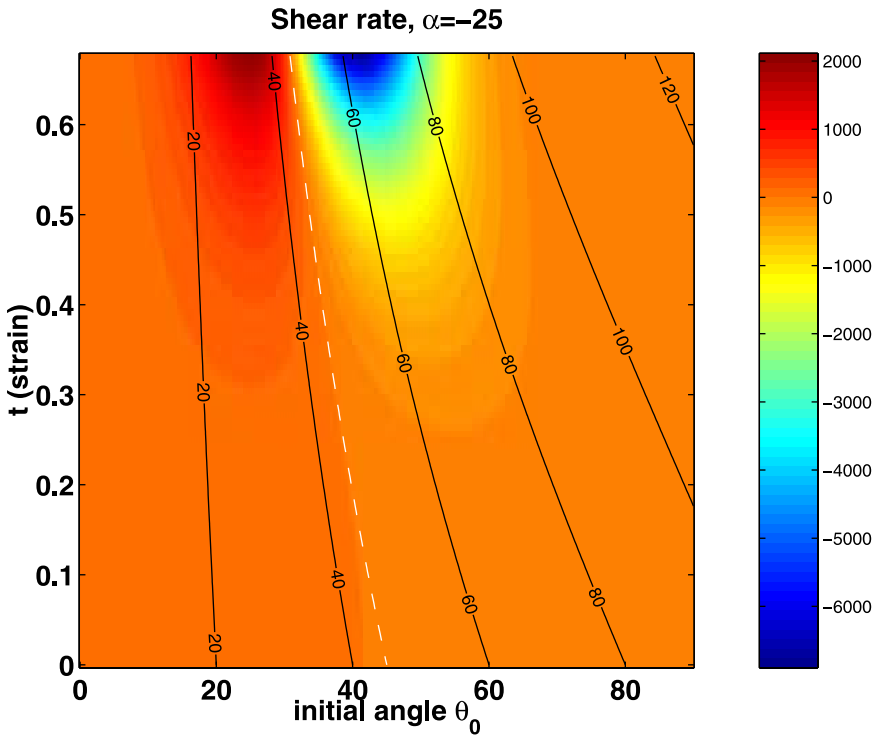

Figure 7. Rate of shear for strongly porosity weakening material $\alpha = -25$ as a function of time and initial angle (colored field). Black contours show the final angle achieved by a given θ_0 at any time t. Positive regions for $\theta_f < 45°$ have shear in the same sense as the overall simple shear. Negative regions for $\theta_f > 45°$ have the opposing sense of shear. The white dashed contour shows $\theta_f = 45°$ where $S(t) = 0$.

normalized shear and growth rates for positive values and again, suggests that only a relatively narrow band of angles (here ~20–30°) have both significant growth and enhanced shear.

4. Discussion

[25] The results of this linear analysis are encouraging and suggest that the theory of flow in deformable porous media should be applicable for explaining and quantifying the laboratory experiments. Nevertheless, there are several important differences between the linearized solutions and the experiments that require further work to explain (although the results of the linear analysis suggest some reasonable solutions).

[26] First, the linearized solutions do not demonstrate a preferred wavelength as is claimed to be seen in the experiments "for the largest melt bands." In the linear analysis, all perturbations with wavelengths shorter than about 0.5 compaction lengths grow at the same rate. This result is the same as *Stevenson* [1989] and may simply arise from the lack of any surface energy terms in the governing equations. At the scale of these experiments (and certainly near the grain scale), surface energy terms should become important and will act as nonlinear diffusive terms that redistribute melt from high porosity regions to low porosity regions [e.g., see *Riley and Kohlstedt*, 1991]. Such a process would reduce the growth of very short wavelength perturbations and give rise to a preferred length scale. Further work to model experimental charges should probably include surface energy effects.

[27] For strongly porosity weakening systems, significant growth in amplitude can occur at strains less than 1. This is consistent with some of the lower porosity experiments ($\phi_0 = 0.02$) which show that the bands are observable at strains as low as 1.1 (although more melt rich systems don't develop bands until strains of ~2 which might imply that there is some porosity

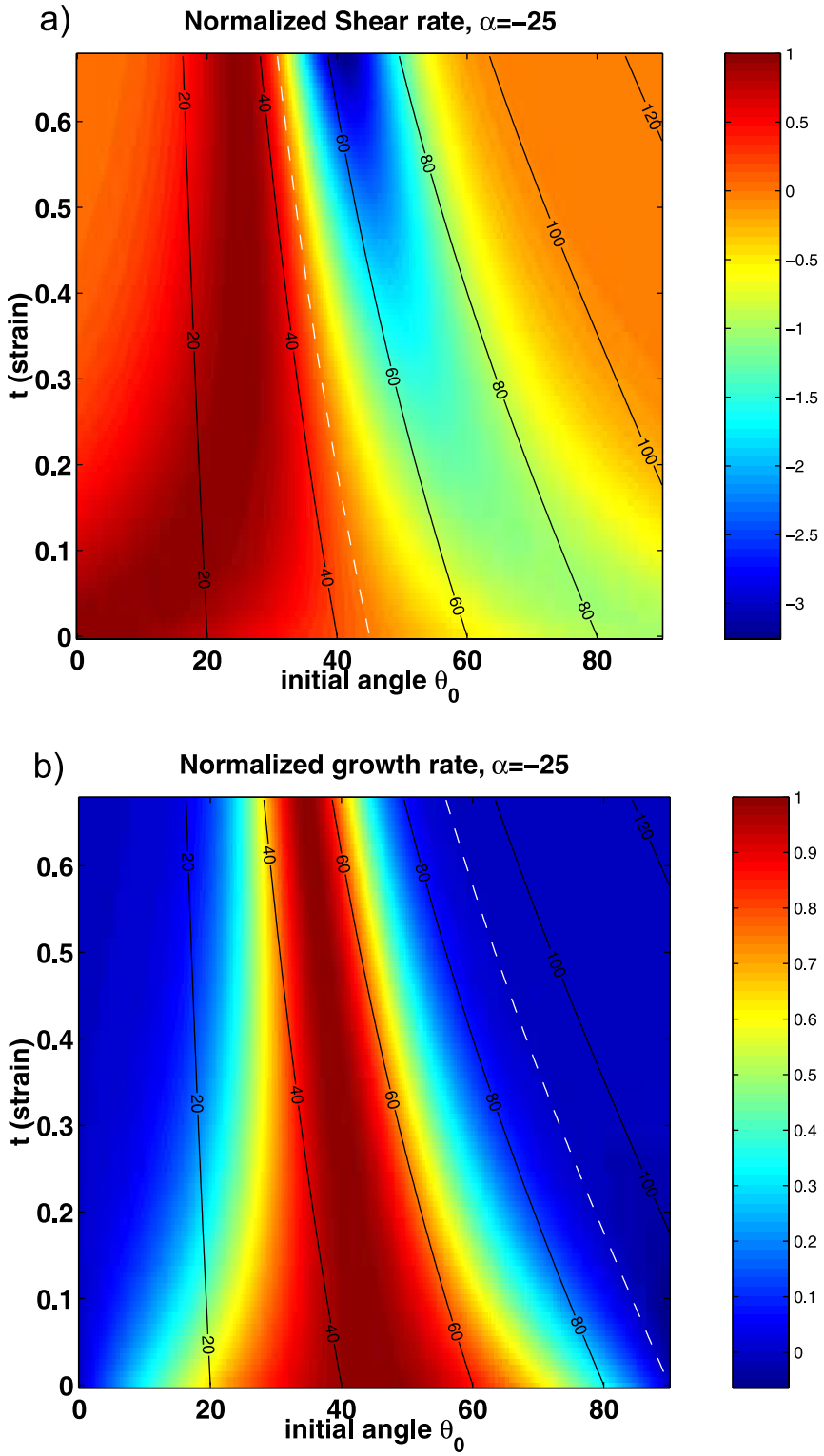

Figure 8. Comparison of normalized shear rate (a) to normalized growth rate (b) for $\alpha = -25$. The maximum rate of shear occurs for low angle waves at ~20–30°, while the maximum growth rate occurs for waves around 45°. If both shear and growth are important for selecting the preferred angle, this analysis suggests that only low angle perturbations have a favorable sense of shear and growth rate. (c) The product of the normalized shear and growth rates (Figures 8a and 8b) just for positive values which gives an indication of the angles over which shear and growth reinforce each other.

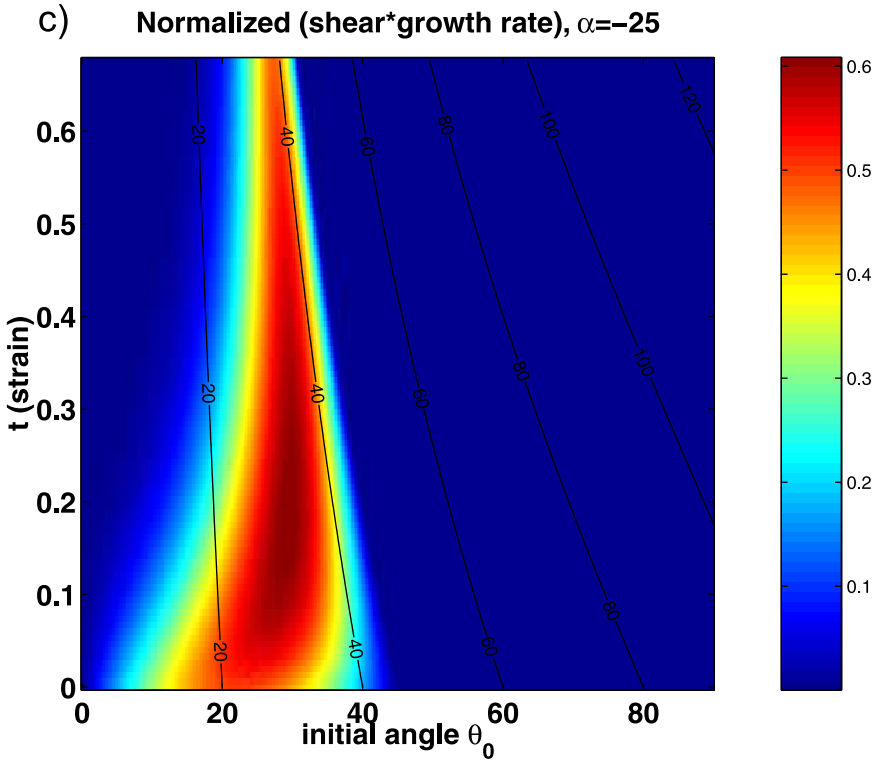

Figure 8. (continued)

dependence in α). The most noticable difference between theory and experiment, however, is that the experimentally produced melt-rich bands remain at low angles to the shear plane ($\sim 20^\circ$) even after very large amounts of simple shear. In the linearized solutions, the largest growing perturbations begin at low angles but eventually rotate to about $60-80^\circ$ after about a strain of 3 (Figure 4).

[28] Nevertheless, there are several features missing from this analysis that might explain this discrepancy. First, these linearized solutions are for infinite domains whereas the experiments are tightly confined by upper and lower boundaries that are impermeable to both solid and melt flow. Such boundaries should introduce another length scale into the problem as well as impose important constraints on the growth of shear bands. Figures 6–8 suggest that only low-angle melt bands will be favorable for both growth and enhanced right-lateral shear along the melt bands. While higher angle melt bands can still grow, their sense of shear is reversed and would develop significant discrepancies in solid and melt flow at the boundaries and might be suppressed. Future numerical analysis will investigate the possible role of the impermeable boundary conditions.

[29] Finally, the linearized solutions (by definition) do not allow any feedback between the perturbed solid flow field and the melt bands. The growth of porosity is driven completely by the rotations induced by the zeroth order simple shear. In the full nonlinear problem, however, once the bands become sufficiently weak, they become strain guides which redirect the solid flow along the bands rather than through them. This should also reduce the amount of rotation that the bands experience. To find a full solution that couples both shear and porosity growth through decompaction, requires numerical schemes that can accurately solve for both solid and fluid flow in a variable viscosity medium with strongly localized viscosity variations. This in turn requires a variable viscosity, solid flow solver with accurate pressures to calculate the feedback between fluid flow and viscosity variations. Such schemes are likely to be numerically challenging to develop. However, the

existence of well characterized physical experiments should make the development and validation of such codes easier.

Acknowledgments

[30] This work was supported by NSF grant OCE-0207851 to Spiegelman. Many thanks to B. Holtzmann and D. Kohlstedt who provided early preprints of their experimental work as well as insightful discussions and reviews. Thanks also to D. Stevenson and an anonymous reviewer for additional helpful reviews. This is LDEO contribution 6490.

References

Bercovici, D., Y. Ricard, and G. Schubert, A two-phase model for compaction and damage: 1. General theory, *J. Geophys. Res.*, *106*, 8887–8906, 2001a.

Bercovici, D., Y. Ricard, and G. Schubert, A two-phase model for compaction and damage: 3. Applications to shear localization and plate boundary formation, *J. Geophys. Res.*, *106*, 8925–8939, 2001b.

Fowler, A. C., A mathematical model of magma transport in the asthenosphere, *Geophys. Astrophys. Fluid Dyn.*, *33*, 63–96, 1985.

Hirth, G., and D. L. Kohlstedt, Experimental constraints on the dynamics of the partially molten upper mantle: Deformation in the diffusion creep regime, *J. Geophys. Res.*, *100*, 1981–2002, 1995a.

Hirth, G., and D. L. Kohlstedt, Experimental constraints on the dynamics of the partially molten upper mantle: 2. Deformation in the dislocation creep regime, *J. Geophys. Res.*, *100*, 15,441–15,052, 1995b.

Holtzman, B. K., N. J. Groebner, M. E. Zimmerman, S. B. Ginsberg, and D. L. Kohlstedt, Stress-driven melt segregation in partially molten rocks, *Geochem. Geophys. Geosyst.*, *4*(5), 8607, doi:10.1029/2001GC000258, 2003.

Kelemen, P. B., G. Hirth, N. Shimizu, M. Spiegelman, and H. J. B. Dick, A review of melt migration processes in the adiabatically upwelling mantle beneath oceanic spreading ridges, *Philos. Trans. R. Soc. London Ser. A*, *355*, 283–318, 1997.

McKenzie, D., The generation and compaction of partially molten rock, *J. Petrol.*, *25*, 713–765, 1984.

Mei, S., W. Bai, T. Hiraga, and D. Kohlstedt, Influence of melt on the creep behavior of olivine-basalt aggregates under hydrous conditions, *Earth Planet. Sci. Lett.*, *201*, 491–507, 2002.

Renner, J., K. Visckupic, G. Hirth, and B. Evans, Melt extraction from partially molten peridotites, *Geochem. Geophys. Geosyst.*, *4*(5), 8606, doi:10.1029/2002GC000369, 2003.

Ricard, Y., D. Bercovici, and G. Schubert, A two-phase model for compaction and damage: 2. Applications to compaction, deformation, and the role of interfacial surface tension, *J. Geophys. Res.*, *106*, 8907–8924, 2001.

Riley, G. N., and D. L. Kohlstedt, Kinetics of melt migration in upper mantle-type rocks, *Earth Planet. Sci. Lett.*, *105*, 500–521, 1991.

Scott, D. R., The competition between percolation and circulation in a deformable porous medium, *J. Geophys. Res.*, *93*, 6451–6462, 1988.

Scott, D. R., and D. Stevenson, Magma solitons, *Geophys. Res. Lett.*, *11*, 1161–1164, 1984.

Scott, D. R., and D. Stevenson, Magma ascent by porous flow, *J. Geophys. Res.*, *91*, 9283–9296, 1986.

Spiegelman, M., Flow in deformable porous media: Part 1. Simple analysis, *J. Fluid Mech.*, *247*, 17–38, 1993a.

Spiegelman, M., Flow in deformable porous media: Part 2. Numerical analysis—The relationship between shock waves and solitary waves, *J. Fluid Mech.*, *247*, 39–63, 1993b.

Spiegelman, M., and D. McKenzie, Simple 2-D models for melt extraction at mid-ocean ridges and island arcs, *Earth Planet. Sci. Lett.*, *83*, 137–152, 1987.

Stevenson, D. J., Spontaneous small-scale melt segregation in partial melts undergoing deformation, *Geophys. Res. Lett.*, *16*, 1067–1070, 1989.

Whitham, G., *Linear and nonlinear waves*, John Wiley, New York, 1974.

Zimmerman, M. E., S. Q. Zhang, D. L. Kohlstedt, and S. Karato, Melt distribution in mantle rocks deformed in shear, *Geophys. Res. Lett.*, *26*, 1505–1508, 1999.